Single exosome study reveals subpopulations distributed among cell lines with variability related to membrane content

Zachary J. Smith, Changwon Lee, Tatu Rojalin, Randy P. Carney, Sidhartha Hazari, Alisha Knudson, Kit Lam, Heikki Saari, Elisa Lazaro Ibañez, Tapani Viitala, Timo Laaksonen, Marjo Yliperttula & Sebastian Wachsmann-Hogiu

ORIGINAL RESEARCH ARTICLE

Single exosome study reveals subpopulations distributed among cell lines with variability related to membrane content

Zachary J. Smith[1,2], Changwon Lee[1§], Tatu Rojalin[1,3§], Randy P. Carney[4§], Sidhartha Hazari[4], Alisha Knudson[4], Kit Lam[4], Heikki Saari[3], Elisa Lazaro Ibañez[3], Tapani Viitala[3], Timo Laaksonen[3], Marjo Yliperttula[3] and Sebastian Wachsmann-Hogiu[1,5*]

[1]Center for Biophotonics, University of California Davis, Sacramento, CA, USA; [2]Department of Precision Mechanics and Precision Instrumentation, University of Science and Technology of China, Hefei, Anhui, China; [3]Division of Pharmaceutical Biosciences, Centre for Drug Research, University of Helsinki, Helsinki, Finland; [4]Department of Biochemistry and Molecular Medicine, University of California Davis, Sacramento, CA, USA; [5]Department of Pathology and Laboratory Medicine, University of California Davis, Sacramento, CA, USA

Current analysis of exosomes focuses primarily on bulk analysis, where exosome-to-exosome variability cannot be assessed. In this study, we used Raman spectroscopy to study the chemical composition of single exosomes. We measured spectra of individual exosomes from 8 cell lines. Cell-line-averaged spectra varied considerably, reflecting the variation in total exosomal protein, lipid, genetic, and cytosolic content. Unexpectedly, single exosomes isolated from the same cell type also exhibited high spectral variability. Subsequent spectral analysis revealed clustering of single exosomes into 4 distinct groups that were not cell-line specific. Each group contained exosomes from multiple cell lines, and most cell lines had exosomes in multiple groups. The differences between these groups are related to chemical differences primarily due to differing membrane composition. Through a principal components analysis, we identified that the major sources of spectral variation among the exosomes were in cholesterol content, relative expression of phospholipids to cholesterol, and surface protein expression. For example, exosomes derived from cancerous versus non-cancerous cell lines can be largely separated based on their relative expression of cholesterol and phospholipids. We are the first to indicate that exosome subpopulations are shared among cell types, suggesting distributed exosome functionality. The origins of these differences are likely related to the specific role of extracellular vesicle subpopulations in both normal cell function and carcinogenesis, and they may provide diagnostic potential at the single exosome level.

Keywords: *exosomes*; *microvesicles*; *single particle*; *Raman*; *laser trap*; *membrane content*

Responsible Editor: Marca Wauben, Utrecht University, Netherlands.

*Correspondence to: Sebastian Wachsmann-Hogiu, 2700 Stockton Blvd. Suite 1400, Sacramento, CA 95817, Email: swachsmann@ucdavis.edu

To access the supplementary material to this article, please see Supplementary files under 'Article Tools'.

Exosomes are nanosized extracellular vesicles (EVs) formed by nearly all types of cells of intracellular multivesicular bodies (MVBs). They are released into the extracellular space when the MVBs fuse with the plasma membrane. Recently, they have been intensely studied due to discoveries that exosomes (a) transport functional mRNA, miRNA, (1,2) and DNA (3); (b) are expressly packaged by cells for highly specific endogenous and exogenous intercellular communication (4); (c) are constitutively integrated in immune cell physiology (5); and (d) are heavily implicated in numerous pathologies, particularly cancer (6,7). Exosome secretion is also now understood to be fundamental in healthy intercellular communication, and exosomes can be isolated from most

---

§These authors contributed equally to this manuscript.

biological fluids (blood, urine, lymph, etc.) for potential use as biomarkers, since their protein, lipid, genetic, and metabolic content, in addition to frequency of generation, can be altered in diseased cells. Based on the clear evidence that cells actively direct the packing of lipids, protein, RNA, and various cytosolic small metabolites into exosomes, we sought to apply broad chemical spectroscopy to single exosomes for the identification of chemically distinct subpopulations arising from sorting choices during exosome biogenesis or post-translational modification of exosomes after synthesis/release.

Many factors may contribute to perceived chemical dispersity for single exosomes, including exosome isolation techniques (e.g. differential centrifugation vs. commercial precipitation reagents may isolate disparate levels of exosome subpopulations) and also biological mechanisms. For example, exosomal transmembrane proteins exist in various states of post-translational modification [e.g. glycosylation (8)] or lipid/sterol activation (9,10). Finally, while we follow the ISEV characterization guidelines to ensure that the vesicles studied in this paper are exosomes [as opposed to microvesicles (MVs) and other EVs] (11), even this definition is rapidly evolving and may not be soon applicable, hence the continued importance of studies that better define exosomes and their subpopulations.

To explore the chemical content of individual EVs, we utilized Laser tweezers Raman spectroscopy (LTRS). Raman spectroscopy is a well-established, non-destructive, and non-contact method for determining the chemical makeup of a variety of samples (12). Its label-free nature makes it a natural choice for *in vivo* diagnostics and longitudinal studies of cells and tissues over time (13,14). Raman spectroscopy has been successfully applied to a variety of biomedical problems, including cancer detection (15,16), studies of bone health (17,18), response of cells to drugs (19), and quantification of analytes in biofluids (20,21), among many others (22,23).

Among the many forms of Raman spectroscopy, LTRS holds particular promise for study of exosomes. In LTRS, a tightly focused laser beam traps and holds small particles at the laser's focal point. A confocal detection setup collects Raman scattering only from a precise focal volume, allowing cellular and subcellular objects to be studied individually. This method has been used to study, for example, individual cancerous and non-cancerous cells (24,25), the activation response of individual immune cells (26), as well as smaller, nanoscale objects such as lipid droplets in milk (27), latex beads (28), and subcellular organelles (29). These studies highlight the power of Raman spectroscopy to determine the chemical content from individual micro- and nanoparticles, which are well below the limit of detection for conventional "wet chemistry" methods that require a large amount of starting material for analysis. A prior study examined clusters of exosomes, trapped simultaneously in the laser focus, using LTRS, with the disadvantage of obtaining population-averaged information (30). This study found ensemble exosomal chemical differences following cell starvation, highlighting Raman spectroscopy's ability to discriminate between different exosome subpopulations (30). Here, we used LTRS to examine *single* exosomes and MVs isolated from both cancerous and non-cancerous cells to characterize their heterogeneity in chemical content. In this study, exosomes were isolated using both commercial isolation reagents and ultracentrifugation, whereas MVs were separated via ultracentrifugation. Because of the overlapping size distribution of exosomes and MVs when purified with ultracentrifugation, we define *MVs* as those vesicles pelleted at $20,000 \times g$, whereas *exosomes* are those vesicles pelleted at $110,000 \times g$.

By analysing the Raman spectra of many individual exosomes derived from a multitude of cell lines, we were able to identify several subpopulations of exosomes that appeared to be shared across cell lines, suggesting conserved biological function. Additionally, cancerous and non-cancerous cell types appear to differ in relative production of exosome subpopulations, as identified by principal component analysis (PCA). Furthermore, we compared the spectral differences found by PCA to known membrane constituents as well as to principal components derived from a data set consisting of native and trypsinized EVs. This comparison revealed that the dominant chemical differences between these subpopulations are mostly reflected in the content of the EVs' membranes. These results provide information about exosome variability at the single vesicle level that will further elucidate the role of exosome subtypes with regard to their phenotype and ultimate biological function.

Materials and methods

Raman spectroscopy of single extracellular vesicles
Setup and spectral acquisition
As described below, exosomes were first isolated from cell culture and measured one at a time using our Raman trapping system, as shown schematically in Fig. 1. All measurements were made using the home-built LTRS system described previously (14,19). Briefly, 25 mW of light from a single mode, 785 nm laser (CrystalLaser, Reno, NV), was coupled into an inverted microscope (IX-71, Olympus, Center Valley, PA) outfitted with a $60 \times$, 1.2-NA water immersion objective. The light was focused by the objective to a diffraction-limited spot ($\sim 1\,\mu m \times 1\,\mu m \times 3\,\mu m$ in size), capable of trapping cells and other small particles such as lipid droplets and exosomes (14,27). The trapping laser additionally excited Raman scattering from the trapped object, and backscattered light was collected back through the objective. A dichroic beam-splitter and edge filter
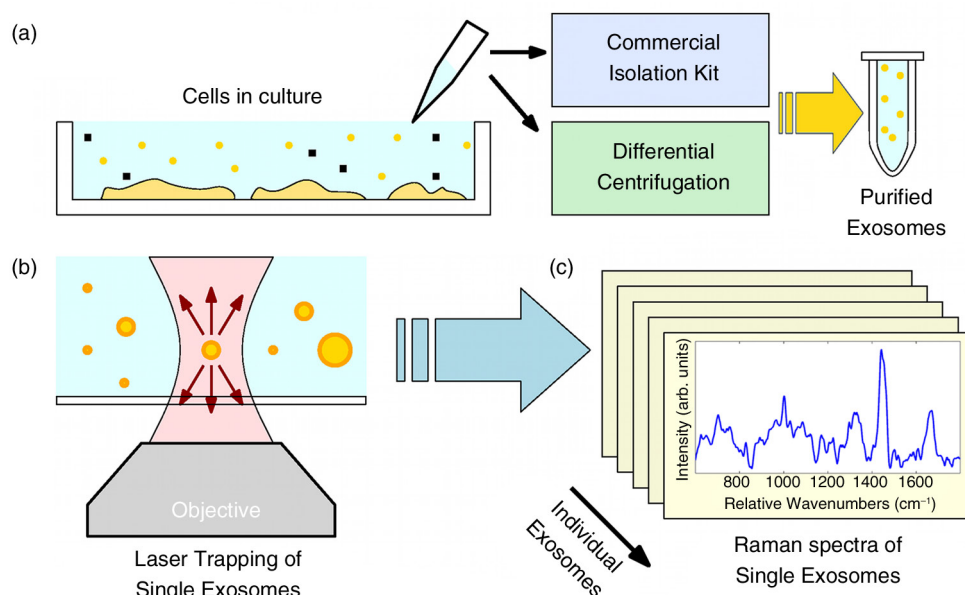
Fig. 1. Schematic diagram of exosome isolation and measurement of single-exosome Raman spectra. (a) Media from cultured cells are purified using a commercial isolation kit or differential centrifugation; (b) purified exosomes are trapped in the laser beam of a home-built microscope system, and Raman spectra are collected, yielding (c) a database of spectra of single exosomes.

(Chroma Technology, Bellows Falls, VT) separated the Raman scattered light from the backscattered excitation light. The filtered Raman signal was focused into a multi-mode optical fibre where it was delivered to a SpectraPro 2300i spectrograph (Princeton Instruments, Trenton, NJ). The dispersed spectrum was measured by a TE-cooled Pixis 100 CCD (Princeton Instruments).

After vesicle preparation, suspensions were diluted 10–100 times in PBS and placed on a quartz coverslip, used to avoid the strong spectral background from glass. The specific dilution factor for each sample was chosen empirically with the goal of having, on average, <1 EV per field of view of the microscope at any 1 time. This step helped to ensure that only single EV particles were measured by our Raman system and to decrease the chance that a second vesicle would wander into the trapping laser beam during spectral acquisition. In order to acquire a spectrum, the stage was manually steered to trap an exosome or MV in solution. The vesicle was levitated away from the quartz coverslip to reduce the signal strength of the substrate. The small volume of the vesicles and the correspondingly small amount of material contained within them necessitated long exposure times to acquire spectra with acceptable signal-to-noise ratios. In our experiments, we recorded ten 30-s spectral frames from each particle.

Following data collection, spectra were imported into MATLAB for all subsequent data processing, described below.

Spectral data processing
All spectra were corrected for cosmic rays using a median threshold filter described previously (31). By comparing spectra pixel-wise across the 10 frames, outlier values caused by cosmic rays can be easily detected and their value replaced by the frame-wise median. Following this correction, the 10 frames from each vesicle were averaged for an equivalent integration time of 5 min per vesicle. The spectra were first smoothed using the Whittaker smoother proposed by Eilers (32) with a Lagrange parameter of 5. Following smoothing, the spectra were background corrected by subtracting off the spectral background from quartz, PBS buffer, total exosome isolation reagent (TEIR), and a fifth order polynomial to account for autofluorescence and other background deviations. Coefficients for each component of the estimated background were determined using an asymmetric least squares (AsLS) model, with a value of the asymmetry parameter of $p = 0.001$ (33,34). For exosome samples isolated using the TEIR reagent kit, we found that the reagents remained attached to the exosomes after purification. The TEIR reagents gave an unexpectedly strong signal, whose removal from each exosome spectrum was verified by comparing exosomes isolated using TEIR and those isolated by ultracentrifugation from the same cell culture, as described in the Supplementary File. Following background correction, all spectra were normalized to the area under the curve of the broad peak at $1,450 \, \text{cm}^{-1}$, a stand-in for total organic content and a standard normalization region (26,35). The y-axis of the Raman spectra then represents the proportion of individual chemical groups relative to the total organic content within an individual vesicle. This allows PCA to represent differences in chemical *composition*,

Zachary J. Smith et al.

rather than differences in chemical *concentration*, as might be encountered, for example, between vesicles of identical content but different size.

Principal components analysis was performed using the built-in MATLAB function princomp. Following principal component decomposition, the first 10 principal component scores for each exosome were submitted to hierarchical clustering analysis using Ward's method for creating linkages based on Euclidean pairwise distances. This analysis was performed using MATLAB's built-in function linkage.

In contrast to the fits of background spectra to the raw spectral data, which were performed with AsLS fitting, fits of principal component spectra shown in the Supplementary File (36) were performed via standard least-squares modelling.

Extracellular vesicle preparation and isolation using the TEIR reagent kit
Cell culture
Human lung carcinoma A549 cell line, human hepatocarcinoma Huh-7 cell line, and mouse embryonic fibroblast 3T3 cell line were cultured in Dulbecco's modified Eagle medium with 10% foetal bovine serum (FBS), 100 units/mL penicillin, and 100 µg/mL streptomycin. Human lung normal fibroblast IMR90 cell line was cultured in Eagle's minimum essential medium with 10% FBS, 100 units/mL penicillin, and 100 µg/mL streptomycin. Human ovarian carcinoma SKOV3 cell line was cultured in McCoy's 5A modified medium with 10% FBS, 100 units/mL penicillin, and 100 µg/mL streptomycin. Human acute T-cell leukaemia Jurkat cell line and human acute myeloblastic leukaemia Kasumi-1 cell line were cultured in RPMI-1640 medium with 10% FBS, 100 units/mL penicillin, and 100 µg/mL streptomycin at 37°C and 5% CO_2. All cell lines were cultured at 37°C and 5% CO_2 and were maintained by splitting upon reaching 80% confluence.

Exosome isolation using commercial precipitation reagent
Exosomes were isolated from cell-conditioned media as previously described (37). Briefly, cells were plated at ~25% confluency in a T-150 flask and incubated in appropriate conditioned medium (CM). CM contained exosome-depleted FBS (bovine-derived exosomes were removed from 30% FBS/media by ultracentrifugation at $100,000 \times g$ for 18 h) to ensure that the resulting exosomes in the cell culture medium originated from the plated cells. After 48 h, the cell culture media was collected and centrifuged at $300 \times g$ for 10 min, $2,000 \times g$ for 20 min, and $10,000 \times g$ for 1 h, to remove live cells, dead cells, and cell debris/MVs, respectively.

The exosome-containing CM was incubated with one-half the total volume of TEIR (4478359; Life Technologies®, Grand Island, NY, USA) at 4°C overnight before final centrifugation at $10,000 \times g$ for 1 h at 4°C. The supernatant was aspirated to waste and the exosome pellet was resuspended in 1 × phosphate-buffered saline (PBS). These exosomes were used in downstream analysis and were stored at −20°C until thawing just prior to use. Exosomes were stored typically for less than 1 week at −20°C and never for longer than 4 weeks.

Preparation of LNCaP exosomes and MVs via differential centrifugation, treatment with trypsin
Cell culture
LNCaP prostate cancer cell line was used as the source for EVs. The cells were grown at +37°C and 5% CO_2 humidified atmosphere in RPMI-1640 medium supplemented with 10% EV-cleared FBS, 20 units/mL of penicillin, and 20 µg/mL of streptomycin (Gibco Invitrogen, Carlsbad, CA). The EV-cleared FBS was prepared by overnight (20 h) ultracentrifugation at $110,000 \times g$ and +4°C of regular FBS using an L-70 ultracentrifuge with rotor type 50.2 Ti (Beckman Coulter, Brea, CA) with approximately 22 mL of supernatant per adaptor tube as described in Ref. (38). The FBS supernatant was then collected and filtered through a 0.22-µm Steritop filter device (Millipore, Billerica, MA). The cells were maintained at 60–90% confluence in T-175 cell culture flasks with 25 mL of medium, and CM was collected after 2–3 days of culture 3 times per week.

Vesicle isolation using differential centrifugation
EVs were isolated from cell-conditioned medium using a differential centrifugation protocol as described previously (3). After collection, any cells and large debris were removed from the CM by centrifugation at $2,500 \times g$ and +4°C for 25 min in 50 mL Falcon tubes with an Eppendorf Centrifuge 5810 R with swinging bucket rotor (Hamburg, Germany). The supernatant was then centrifuged at $20,000 \times g$ and +4°C for 1 h to pellet MVs using a Sorvall RC 5C centrifuge with SLA-1500 rotor (Thermo Scientific, Waltham, MA) with approximately 125 mL of supernatant per adapter tube. The pellet (MVs) was suspended in 100 µL of Dulbecco's PBS buffer (DPBS, Gibco Invitrogen) and the supernatant was centrifuged at $110,000 \times g$ and +4°C for 2 h to pellet exosomes using L-70 ultracentrifuge with Type 50.2 Ti rotor with approximately 22 mL of supernatant per adaptor tube. Because of the overlapping size distributions of the exosomes and MVs, and because of the confusion that still exists about the exact nature of these vesicles' characteristics and defining properties, we adopt the convention in this paper that all vesicles pelleted at $20,000 \times g$ are referred to as *MVs*, whereas those pelleted at $110,000 \times g$ are referred to as *exosomes*. The clear separation obtained between these 2 populations as probed by Raman spectroscopy confirms that these preparation protocols do isolate distinct EV subpopulations. After the ultracentrifugation, the supernatant was removed and the pellets (EVs) were collected with 100 µL of DPBS. The collected EV samples were then

stored in -20°C for short-term (maximum 1 week) storage. Three MV and exosome samples collected during 1 week were pooled together, suspended into a total volume of 1 mL with DPBS and concentrated by ultracentrifugation at $170,000 \times g$ and $+4^{\circ}$C for 3 h using an Optima MAX-XP ultracentrifuge with a TLA-55 rotor (Beckman Coulter). The supernatant was removed from the EV pellets, leaving 30–50 μL to resuspend the pellets, after which they were stored in -80°C.

Cleavage of surface proteins by trypsin treatment
To cleave the membrane protein segments outside of the EVs, the EV samples were incubated in 1 mL of 0.25% (w/v) trypsin (Gibco Invitrogen) in DPBS for 1 h in $+37^{\circ}$C. One-half of each sample was treated with trypsin and the other half served as a point of comparison for the effect of the treatment. The effect of trypsin treatment was assessed by western blotting of membrane proteins CD9 and CD63 as described below (39).

Size-exclusion chromatography
The trypsin-treated EVs and their control samples were purified by size-exclusion chromatography to separate the trypsin, cleaved protein segments, and other small molecules from the EVs as described by Boing et al. (40). For each sample, a column was prepared with 10 mL of sepharose CL-2B (GE Healthcare Life Sciences, Little Chalfont, UK) in DPBS running buffer, both degassed under vacuum. The samples were loaded into the column and 11 fractions of 0.5 mL were collected immediately from the start of the run. The presence of small particles in the fractions was confirmed with NTA (see below) from Fractions 7–10, with the highest particle concentrations usually found in Fractions 8 and 9. Fractions 7–10 were then pooled together and concentrated by ultracentrifugation at $170,000 \times g$ as described above.

EV characterization
Electron microscopy of exosomes and EVs
TEIR-isolated vesicles were diluted in $1 \times$ PBS and re-pelleted at $100,000 \times g$ for direct resuspension in 2% (w/v) paraformaldehyde with 5 μL being deposited on Formvar carbon-coated EM grids. The grids were washed, transferred to 1% glutaraldehyde, contrasted in a solution of uranyl oxalate, and then contrasted and embedded in methyl cellulose–uranyl acetate according to a previously reported methodology (37). The grids were examined in a Philips/FEI BioTwin (Amsterdam, Netherlands) CM120 transmission electron microscope at 80 kV. Representative images from A549 exosomes are shown in Fig. 2a (left), showing the expected cup-shaped morphology.

For LNCaP, MVs both treated with trypsin and untreated were imaged by cryo-electron microscopy. Then, 3 μL of concentrated EV samples was added onto carbon TEM grids purified with a Gatan Solarus (Model 950) plasma cleaning system and frozen with Vitrobot (FEI) in liquid nitrogen. The grids were analysed by a JEOL JEM-3200FSC field emission cryo-TEM with 170 kV. Results are shown in Fig. 2a (middle, right), where the native circular morphology is seen in both treated and untreated MVs.

Immunoblot analysis to confirm exosome isolation
For exosomal western blots, 40 μg exosome aliquots were lysed in SDS sample buffer: 2% (w/v) sodium dodecyl sulphate, 125 mM Tris–HCl, pH 6.8, 12.5% (v/v) glycerol, and 0.02% (w/v) bromophenol blue. They were incubated with 50 mM DTT where necessary (i.e. not for anti-CD9 and anti-CD63 probing), heated for 5 min at 95°C, and spun to precipitate insoluble material (2 min, $14,000 \times g$). Protein was loaded onto gels according to the concentration as measured by BCA assay (Pierce, Rockford, IL), by first assuring no worse than "low" purification according to the ratio of vesicle counts by NTA to protein concentration (41). For whole cell lysates, cells were lysed in RIPA buffer (Thermo Scientific) with protease inhibitor and centrifuged at $18,000 \times g$ at 4°C for 30 min to remove cell debris, and protein concentration of the cleared supernatants was determined by BCA assay. Exosomal and whole cell lysate proteins (20 μg per lane) were subjected to electrophoresis on 1-mm 10-well NuPAGE 4–12% (w/v) Bis-Tris Precast gels (Thermo-Fisher Scientific) performed at 90 V for 30 min and then 120 V until complete in NuPage MOPS buffer using an Xcell Surelock™ gel tank (ThermoScientific). Following electrophoresis, the proteins were transferred onto nitro-cellulose membranes (ThermoFisher Scientific) for 2 h at 4°C and subsequently probed with the following anti-bodies: mouse monoclonal anti-CD63 (ThermoFisher Scientific), mouse monoclonal anti-CD9 (ThermoFisher Scientific), rabbit polyclonal anti-tsg101 (Sigma–Aldrich, St. Louis, MO, USA), and rabbit polyclonal anti-calnexin (Cell Signaling Technology, Danvers, MA, USA). Secondary antibodies (HRP-conjugated) were goat anti-rabbit and goat anti-mouse immunoglobulin (Santa Cruz Biotechnology, Dallas, TX, USA). All antibodies were prepared fresh at 1:1,000 dilutions (except anti-tsg101 at 1:500) in 5% (w/v) non-fat dairy milk in Tris-Buffered Saline with Tween™ (TBST) buffer (also used to block membranes). Immuno-active bands were detected on a (Bio-Rad ChemiDoc™: Hercules, CA, USA) MP Imaging System after 5 min ECL substrate incubation. Blots were re-probed as necessary to conserve exosome protein. The results of the western blot (shown in Fig. 2b) are consistent with exosome properties and thus validate the collection methodology used in this manuscript.

Immunoblot analysis to confirm digestion of surface proteins by trypsin
EV samples and cell lysates were lysed with RIPA buffer in the presence of a protease inhibitor mixture (Sigma–Aldrich) and prepared with $2 \times$ Laemmli buffer (Bio-Rad) in non-reducing conditions. Using SDS–polyacrylamide
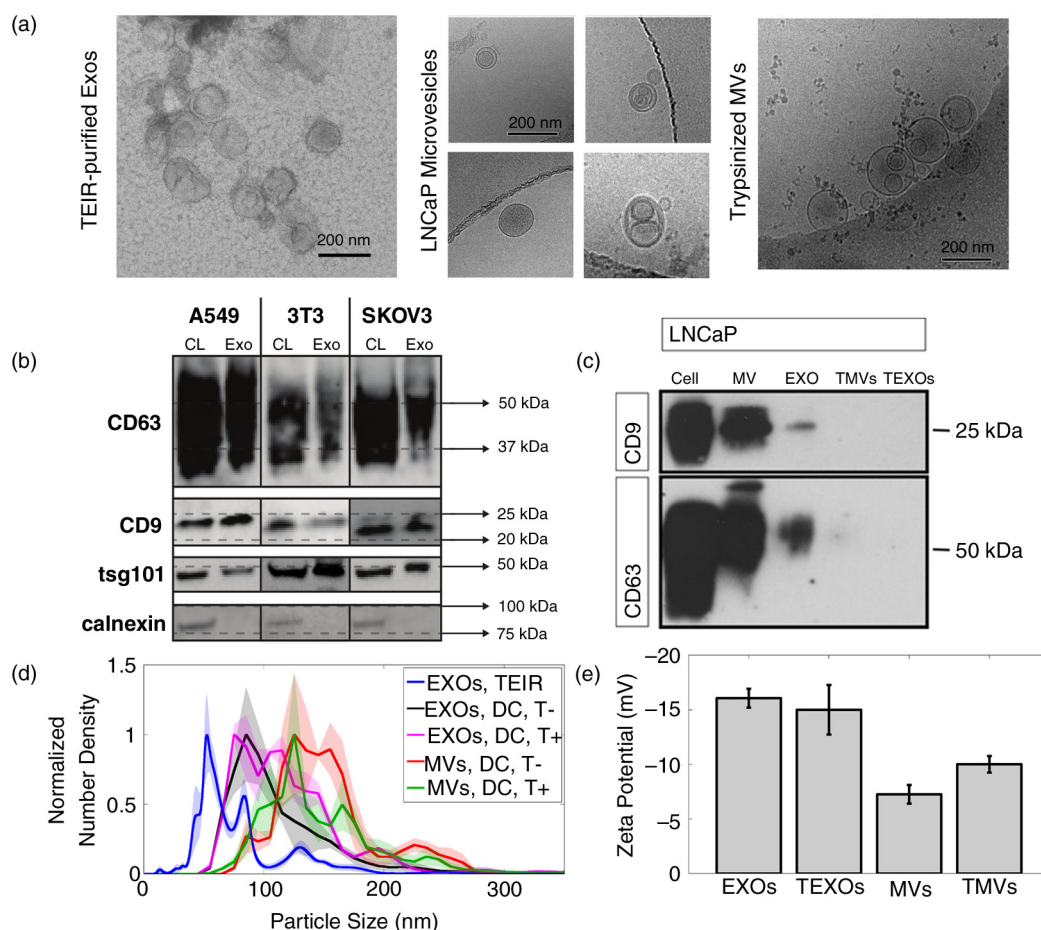
Zachary J. Smith et al.

Fig. 2. Characterization of extracellular vesicles by electron microscopy, Western blot, κ-potential, and nanoparticle tracking analysis (NTA). (a) Electron micrographs of exosomes purified by total exosome isolation reagent (TEIR) (left, conventional TEM showing cup-shaped morphology), vesicles purified by differential centrifugation (middle, Cryo-EM showing native circular morphology), and trypsin-treated vesicles (right, cryo-EM). (b) Western blots of CD63, CD9, tsg101, and calnexin from exosomes and cell lysates for 3 representative cell lines (20 μg per lane). (c) Western blot of CD9 and CD63 for LNCaP microvesicles (MVs) and exosomes (EXOs) and trypsinized microvesicles (TMVs) and exosomes (TEXOs) (50 μg per lane). (d) Averaged NTA-determined size distributions for exosomes and microvesicles purified by TEIR and differential centrifugation (DC). Shaded areas represent ±1 standard error. (e) κ-potential for LNCaP extracellular vesicles.

gel electrophoresis (PAGE), 50 μg of proteins was separated into 12% Mini-PROTEAN TGX™ gels (Bio-Rad) and transferred to a Protran nitrocellulose membrane (Whatman International Ltd, Kent, United Kingdom) at 100 V and 30 mA for 1 h. Blots were blocked in 5% (w/v) non-fat dry milk powder (Valio, Helsinki, Finland) in Tris-buffered saline Tween 20 (TBS-T) and then incubated for 1 h at room temperature (RT) with either mouse mono-clonal anti-human CD9 (clone ALB 6; Santa Cruz Biotechnology) or anti-CD63 (clone H5C6; BD Phar-mingen™, San Jose, CA, USA), both diluted in 5% non-fat dry milk in TBS-T. The membranes were washed 3× for 10 min and incubated with goat anti-mouse IgG-HRP secondary antibody diluted in 2.5% non-fat dry milk powder in TBS-T for 45 min at RT. The membranes were washed 3× for 10 min with TBS-T, developed using a Luminata™ Crescendo Western HRP Substrate

(Millipore) and visualized with Amersham Hyperfilm™ ECL (GE Healthcare Limited). As shown in Fig. 2c, the LNCaP MVs and exosomes as well as the cell lysates are positive for CD9 and CD63. However, the trypsinization treatment cleaves the cellular surface proteins as shown in the trypsinized microvesicles (TMVs) and exosomes.

Nanoparticle tracking analysis
For the LNCaP cells, purified EV samples were analysed by NTA (36) using Nanosight model LM14 (Malvern, Malvern, UK) equipped with a blue (404 nm) laser and sCMOS camera. The samples were diluted in DPBS to obtain a suitable concentration for the analysis ($3–20 \times 10^8$ particles/mL) and three 90-s videos were recorded from the samples using camera level 13. The data were analysed using NTA 3.0 software with the detection threshold set to 3 and screen gain at 10 to track

as many particles as possible with little background. These settings have been chosen to closely match prior studies that have used NTA to detect exosomes as small as 30 nm (42–44). Results are shown in Fig. 2d, with the solid lines depicting mean distributions across the replicate measurements and the shaded areas showing the standard error. As expected, MVs have a larger mean size compared to the smaller exosome population. Number densities have been normalized to their maximum value.

We also show a characteristic size NTA result obtained from A549 cells isolated by the commercial TEIR reagent as described above (blue curve in Fig. 2d). These data were recorded by a separate NanoSight LM10 instrument (illumination at 488 nm) equipped with a perfusion pump. The A549 sample was diluted $1000\times$ in freshly filtered PBS (filtered using a 0.01-μm filter). The filtered PBS was confirmed via NTA to be free of nanoparticle contamination. Diluted exosome samples were passed 3 times through 0.2-μm nylon syringe filters and placed on the NTA instrument at RT. The blue curve in Fig. 2d represents the average and standard error of 6 consecutive measurements. Each repetition recorded 60 s of data, with 30 s of sample flow between replicates.

Zeta potential measurements

For the LNCaP cells, zeta potentials were measured from the purified EV samples with a Zetasizer Nano Z (Malvern), with 3 replicates measured from each sample. The particle concentrations in the samples were prepared at approximately 5×10^8/mL in DPBS using particle size concentrations obtained by paired NTA, such that each sample had similar particle concentrations. The results are shown in Fig. 2e, where it is evident that exosomes and MVs have distinctly different zeta potentials ($p=8\times10^{-4}$), further providing evidence that the differential centrifugation effectively separated exosomes and MVs.

Results and discussion

Raman spectra of exosomes isolated from 7 cancerous and non-cancerous cell lines

LTRS spectra were recorded from exosomes isolated from 7 cell lines divided among cancerous (5) and non-cancerous (2) lines of epithelial and myeloid origin. A schematic diagram of the experiment is shown in Fig. 1. In Fig. 1a, culture media containing exosomes and other contaminating particles are collected, purified, and concentrated to yield a vial with a dense suspension of exosomes. That sample is then diluted and placed on a home-built Raman microscope, where single exosomes are trapped in a laser beam as shown in Fig. 1b. Raman scattered light is collected from each exosome, yielding a database of Raman spectra (Fig. 1c). Between 10 and 20 exosomes from each cell line were measured, with

the mean spectra and ±1 standard deviation shown in Fig. 3a. The Raman spectra largely resemble those in the literature acquired from single cells and other biological tissues, and the chemical assignment of the major bands in the exosome spectra can be found in Ref. 30. The mean spectra show striking variability between exosomes derived from different cell lines. Several consistent differences can be observed, including (a) the height of the peak at $\sim700\,\mathrm{cm}^{-1}$, which is significantly elevated in the exosomes derived from non-tumour cell lines 3T3 and IMR90, (b) the shape of the $1{,}000–1{,}100\,\mathrm{cm}^{-1}$ and $1{,}200–1{,}300\,\mathrm{cm}^{-1}$ regions, and (c) the $1{,}600–1{,}700\,\mathrm{cm}^{-1}$ region, which distinguishes the A549, SKOV3, and Jurkat lines from the others. These areas are highlighted in Fig. 3a, d, and e, as a visual aid.

Performing a PCA on the full data set reveals principal component loadings that recapitulate the differences that are apparent by visual inspection, as well as other, subtler differences, as shown in Fig. 3d. The chemical assignments for the major features in the principal components are given in Table I.

The first 3 components represent 33, 18, and 10% of the variance, respectively, in the data set. Thus, cumulatively they represent 61% of the total variance. Scores for the first 3 principal component axes are shown in Fig. 3b and c. To avoid confusion with the principal components analysis performed on measurements of trypsin-treated EVs, described in the next section, we give these principal components the subscript "7c" to reflect that they originate from a data set composed of 7 cell lines. In the data set shown in Fig. 3, distinct clusters of exosomes can be identified using hierarchical clustering analysis, performed as described in the Materials and Methods section, using the first 10 principal component scores for each exosome (see Supplementary File).

Based on this hierarchical clustering analysis, each individual exosome was assigned to 1 of 4 clusters based on its spectrum. The cluster membership of each exosome is indicated in Fig. 3b and c by varying symbols, as shown in the legend. Shaded regions are provided as visual aids to highlight the different cluster regions. For example, Cluster 1 is represented by a star symbol and contains the majority of the Jurkat, SKOV3, and A549 exosomes within the region highlighted by the shaded blue oval. Interestingly, the exosomes derived from the 2 non-tumour cell lines (represented by gold and black colour) fall almost exclusively into Clusters 2 and 3 (represented by circles and triangles, respectively). To identify the specific spectral features of each cluster, we plotted the cluster-averaged spectra in Fig. 3e.

The cluster-averaged spectra reveal clear differences between exosomes from different subgroups. Here, the differences between each group are even more pronounced than in the cell-line-averaged spectra in Fig. 3a, as expected given that many cell lines have exosomes in more than
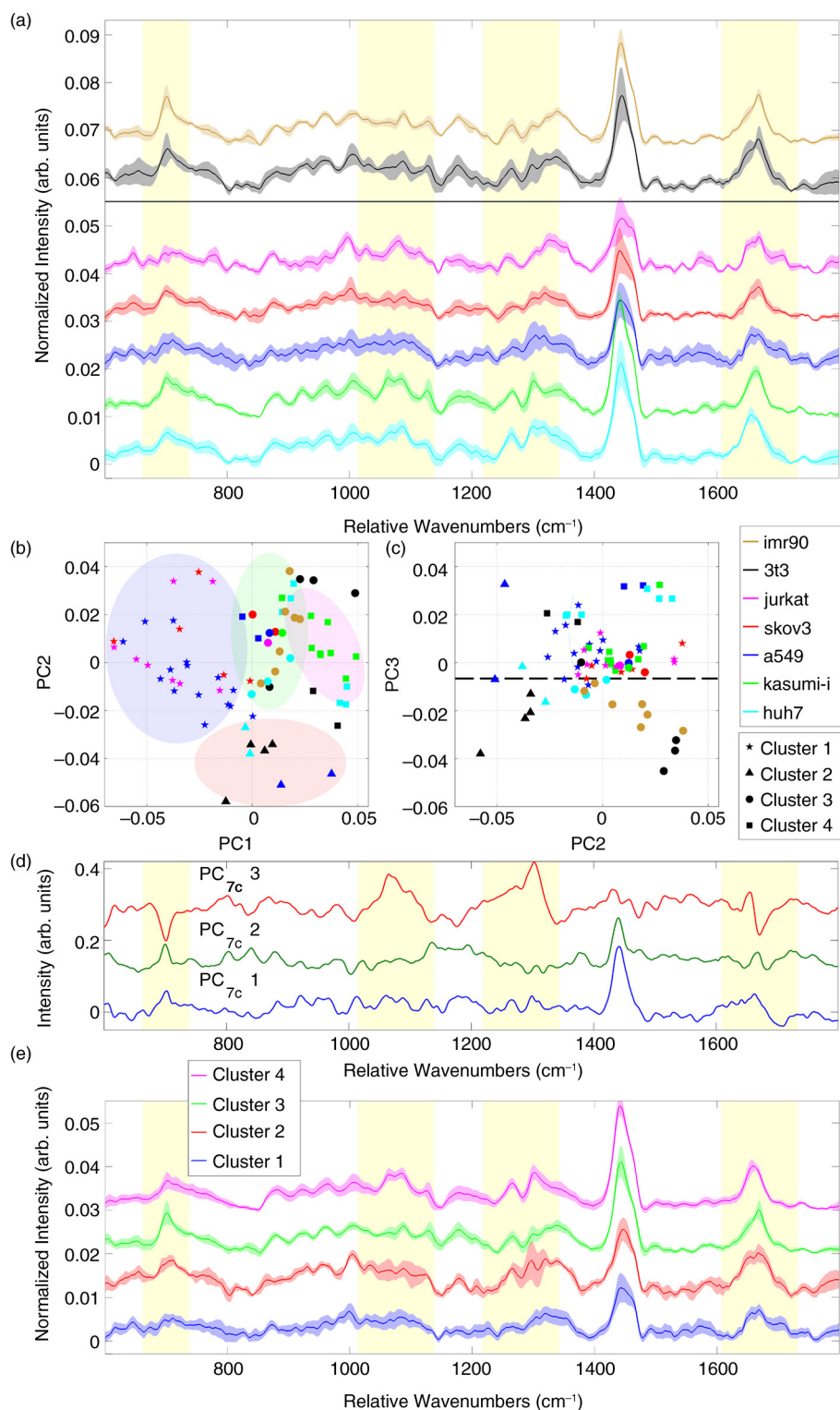
Zachary J. Smith et al.

Fig. 3. Analysis of Raman spectra from single exosomes derived from 7 cancerous and non-cancerous cell lines. (a) Average Raman spectra (solid lines) and ±1 standard deviation (shaded areas) of exosomes. Black line separates normal (imr90, 3t3) and cancerous cell–derived exosomes (others). (b) First and second and (c) second and third principal component scores for each cell line. Colours represent cell lines, whereas shapes represent cluster membership, as shown in the legend (right). Clusters are based on a linkage analysis as described in the Supplementary File. Coloured regions throughout figure and dashed line in (c) provided as visual aids. (d) The first 3 principal component loading vectors, calculated from the full exosome spectral data set from all 7 cell lines. (e) Averaged spectra from Clusters 1 through 4. Spectra in panels (a), (d), and (e) offset for clarity.

Table I. Literature assignments of major spectral features in Fig. 3(d).

Position (cm^{-1})	Peak assignment	Reference
700	Cholesteryl ester	(45)
840	Saccharide/amines	(45,46)
882	Tryptophan side-chain in proteins	(47)
1,066	Chain C–C stretching in lipids	(48)
1,298	CH$_2$ deformations in lipids	(49)
1,450	CH$_2$ and CH$_3$ deformations in proteins and lipids	(49)
1,651	C$=$C stretching in lipids	(50)
1,668	Amide I vibrations in proteins Cholesteryl ester	(45,51)

1 cluster. Because the differences do not correspond to cell type, we hypothesize that there may be several separate classes of exosomes, varying in content and specific biological directive. The preference of each cell line to create exosomes of a given type is likely to be driven by that cell's role within the organism as a whole and to be heavily influenced by the cellular environment (e.g. tumour microenvironment). The paucity of exosomes from normal cell lines in Clusters 1 and 4 suggests that whatever function these exosomes serve is performed with greater frequency in cancerous versus normal cells. In fact, a close inspection of Fig. 3c reveals that the majority of the exosomes from non-tumour cells (black and gold colour) fall on the low end of the PC$_{7c}$ 3 axis. A dashed line is

provided as a visual aid to highlight this discrimination. Identifying the meaning of these principal component axes will allow us to identify what chemical changes are present within each exosome group compared to the others.

Our hypothesis is that the primary spectral differences represented by the first 3 principal component axes are cholesterol content, surface protein expression, and relative expression of phospholipids to cholesterol, respectively. Comparing the major peaks in PC$_{7c}$ 1 to Table I reveals a strong spectral similarity with cholesterol, whereas PC$_{7c}$ 3 shows an inverse relationship between phospholipids and cholesterol [which have been previously shown to have an inverse relationship in exosomal membrane composition (52)]. This hypothesis is further strengthened by comparing these principal components with reference spectra for cholesterol (Sigma–Aldrich, C8667), phosphatidylcholine (Sigma–Aldrich, P3556), and phosphatidylethanolamine (Sigma–Aldrich, P7693), which agree with prior reports in the literature (53), and are provided for visual comparison alongside PC$_{7c}$ 1 and 3 in Fig. 4.

The spectral similarity between the principal components and the spectra of pure chemicals can be quantified through least-squares curve fitting, as described in the Supplementary File. Fitting PC$_{7c}$ 3 with a mixture of cholesterol and phospholipids yields a curve that faithfully reproduces the principal component's major peaks (Pearson's correlation coefficient r$=$0.82; see Supplementary Fig. 4). Since Raman spectroscopy is a quantitative technique whose signal is linear with chemical concentration, the fit coefficients can be used to
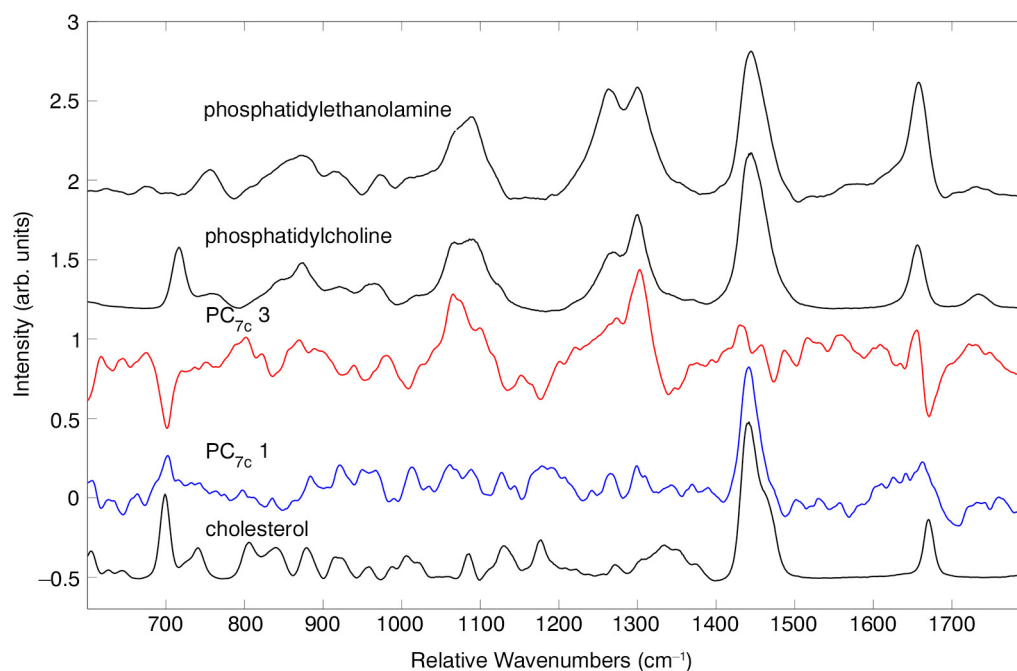

Fig. 4. Comparison of lineshapes of principal components 1 and 3, shown in Fig. 3d, and pure spectra of cholesterol, phosphatidylcholine, and phosphatidylethanolamine (black traces).

determine quantitative relationships between chemicals represented by this principal component. As described in detail in the Supplemental File, the spectral fitting coefficients indicate that PC_{7c} 3 represents a specific exchange ratio between cholesterol and phospholipid, where increasing values on this axis represent phospholipid molecules added to the membrane at the cost of cholesterol, at a 1:1 ratio of cholesterol/phospholipid. Thus, increasing values on the first principal component axis represent increased total cholesterol concentration, while increasing values on the third principal component axis represent an increase in the ratio of phospholipids to cholesterol.

Although this simple comparison of PCs to pure chemical components allows a good understanding of PC_{7c} 1 and PC_{7c} 3, the chemical meaning of the second principal component is not as clear from its overall shape. Comparing its major peaks with those in Table I, we see that the peaks primarily originate from proteins and protein-associated saccharides. Given that cholesterol and phospholipids are membrane components, our hypothesis is that PC_{7c} 2 also represents a membrane component, namely membrane-associated proteins. To confirm our hypothesis that its shape represents surface protein expression, we ran a control experiment where we looked at spectral differences between native and trypsin-treated exosomes, described below.

Raman spectra of extracellular vesicles after treatment with trypsin

Exosomes and MVs were isolated from cultures of LNCaP cells via differential centrifugation of the culture medium as described in the Materials and Methods section. Following isolation, both exosome and MV samples were treated with trypsin, a proteolytic enzyme, to cleave the extracellular portion of most membrane proteins from the surface of the vesicles, leaving them "bald." Trypsin is a digestive enzyme that works by cleaving peptides at certain sites (54), thus breaking large proteins into smaller subunits. Trypsinization is a widely applied technique, used regularly for proteomic sample processing and in cell culture, either to break down cell adhesion proteins or to efficiently strip away surface protein (55). After trypsinization of the EVs isolated in this study [following a previously reported procedure (39)], Western blot analysis (see Materials and Methods section) was used to confirm the removal of tetraspanins CD9 and CD63, transmembrane proteins that are highly expressed at exosomal membranes. Because we found in our previous experiments that purification with the TEIR left a "coating" of the reagent around exosomes (see Ref. (56) and Supplementary File), we used differential centrifugation to purify these vesicles to ensure that the TEIR reagent did not interfere with the digestions of membrane proteins by trypsin.

LTRS spectra were recorded from ~ 7 to 10 vesicles from each group. Both mean spectra and ± 1 standard deviation are shown in Fig. 5a. Subtle spectral differences can be observed between exosomes and MVs, particularly in the region around $1,000\,cm^{-1}$. Differences between trypsinized and native vesicles can also be seen, particularly in the protein- and lipid-rich $1,200–1,400\,cm^{-1}$ region. To quantify these differences, principal components analysis was performed on the data set. The first 3 principal component loadings are shown in Fig. 5b. Here we labelled each PC with the subscript "Tr" to indicate that they are the principal components from the trypsin-treatment data set and to prevent confusion with the PCs from the 7 cell line experiment, above. These 3 loadings explain 30, 19, and 15% of the variance in the data set, respectively. Thus, the 3 loadings cumulatively explain 64% of the total variance. In Fig. 5c we plotted the first 2 principal component scores for each individual vesicle, revealing the magnitude and consistency of the separation between exosomes and MVs and between trypsin-treated and -untreated vesicles.

Figure 5c reveals consistent differences between native exosomes and native MVs, along both the PC_{Tr} 1 and PC_{Tr} 2 axes, which we hypothesize to be related to the membrane composition, given the different intracellular origin of the different vesicle types. Specifically, as these differences disappear after the trypsin treatment, both PCs are likely to be related to membrane protein content. This suggests that PC_{Tr} 1 and PC_{Tr} 2 report on particular surface proteins that both distinguish exosomes and MVs and are removed by trypsin treatment.

Comparing the principal component loadings from this data set to the previous data set of 7 different cell lines reveals startling similarities, as shown in Fig. 6. Although the first PC axes for the 2 experiments look quite different, this is to be expected, as in one experiment the primary differentiator would be expected to be the difference between exosomes and MVs (likely surface protein content), whereas in the other case the differentiator is hypothesized to be related to cholesterol content. The lineshapes of the second and third component loadings are remarkably similar between the 2 experiments (PC_{7c} 2 and PC_{Tr} 2 have a Pearson's correlation coefficient of $r = 0.74$, whereas PC_{7c} 3 and PC_{Tr} 3 have a correlation coefficient of $r = 0.92$). We have *a priori* knowledge that the difference between the trypsin-treated and -untreated vesicles, which lies primarily along the PC_{Tr} 2 axis, is the surface protein content [see Western blot data, Fig. 2c, Materials and Methods section]. The similarity between the second loadings in both data sets strongly suggests that PC_{7c} 2 reports on surface protein expression. However, PC_{Tr} 1 also reports on surface protein expression, and thus PC_{7c} 2 may be a mixture of PC_{Tr} 1 and 2. As shown in the
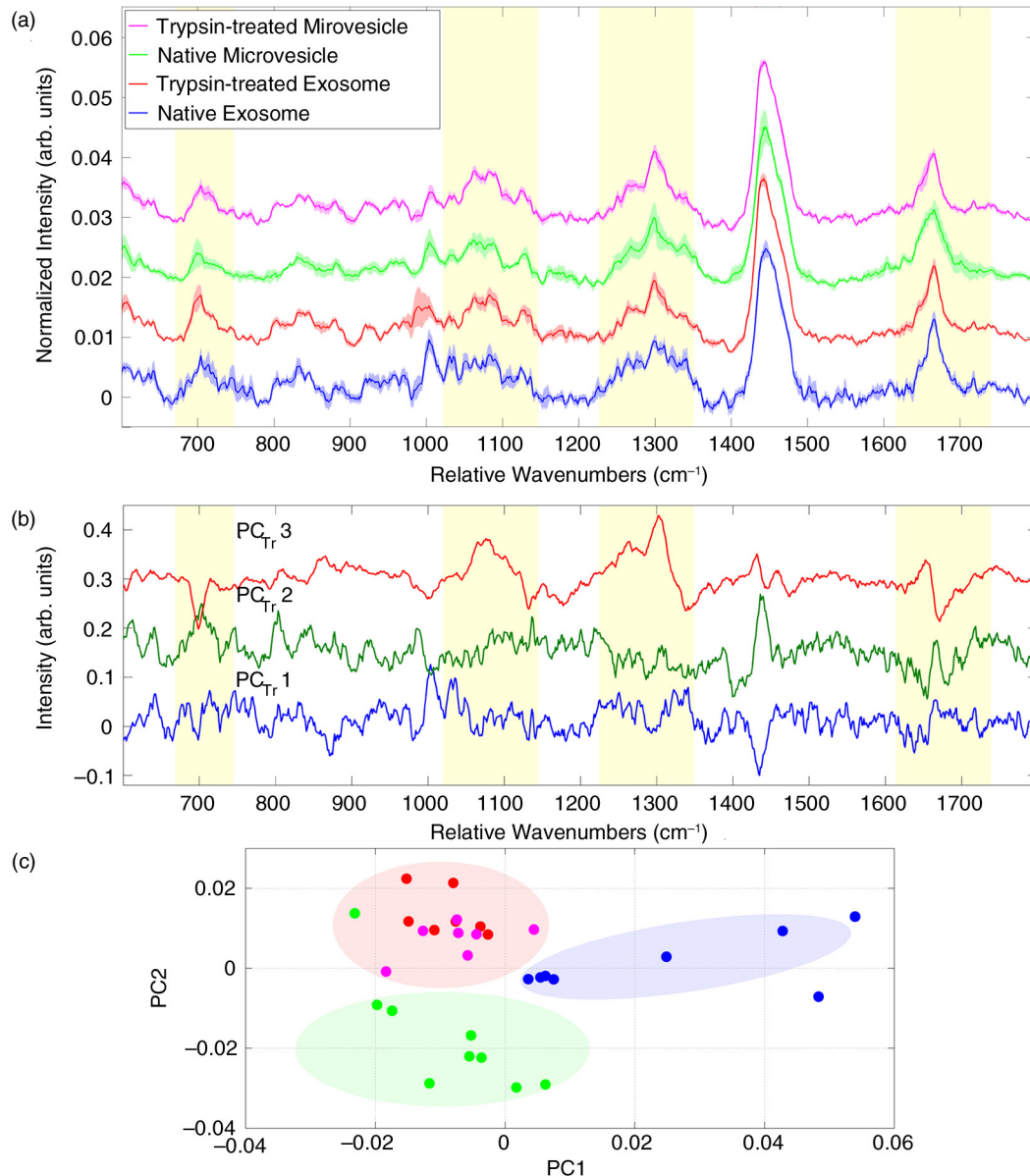
Fig. 5. Analysis of Raman spectra from single LNCaP-derived extracellular vesicles with and without trypsin treatment. (a) Average Raman spectra (solid lines) and ±1 standard deviation (shaded areas). (b) The first 3 principal component loading vectors, calculated from the trypsin-treatment data set. (c) The first 2 principal component scores for individual vesicles, according to the loading vectors shown in (b). Coloured areas in (c) provided as visual aids. Spectra in (a) and (b) offset for clarity.

Supplementary Fig. 5, fitting these curves to PC_{7c} 2 yields a fit that reproduces the major peaks of PC_{7c} 2 (Pearson's correlation coefficient of 0.8). Based on this fit, as well as the position of the trypsinized samples in the PC_{Tr} space (upper left corner, Fig. 5c), we can then hypothesize that increasing values on the PC_{7c} 2 axis corresponds to decreasing surface protein expression.

Conclusions

The current standard practice for exosome analysis relies on bulk isolation and purification from expensive, large-scale *in vitro* cell culture, typically followed by intensive physicochemical analysis, including numerous proteomic, genomic, and sizing techniques. However, it is increasingly clear that conventional analytical tools lack the sensitivity to explore the substantial heterogeneity reported for EVs or are too costly and time-consuming to justify pilot studies. Here, we applied LTRS to truly study the chemical content of exosomes on a vesicle-by-vesicle basis. Additionally, because Raman spectroscopy is a so-called label-free technique, it does not require prior knowledge of, for example, specific surface proteins for fluorophore conjugation and can study EVs in close approximations to their biological milieu.
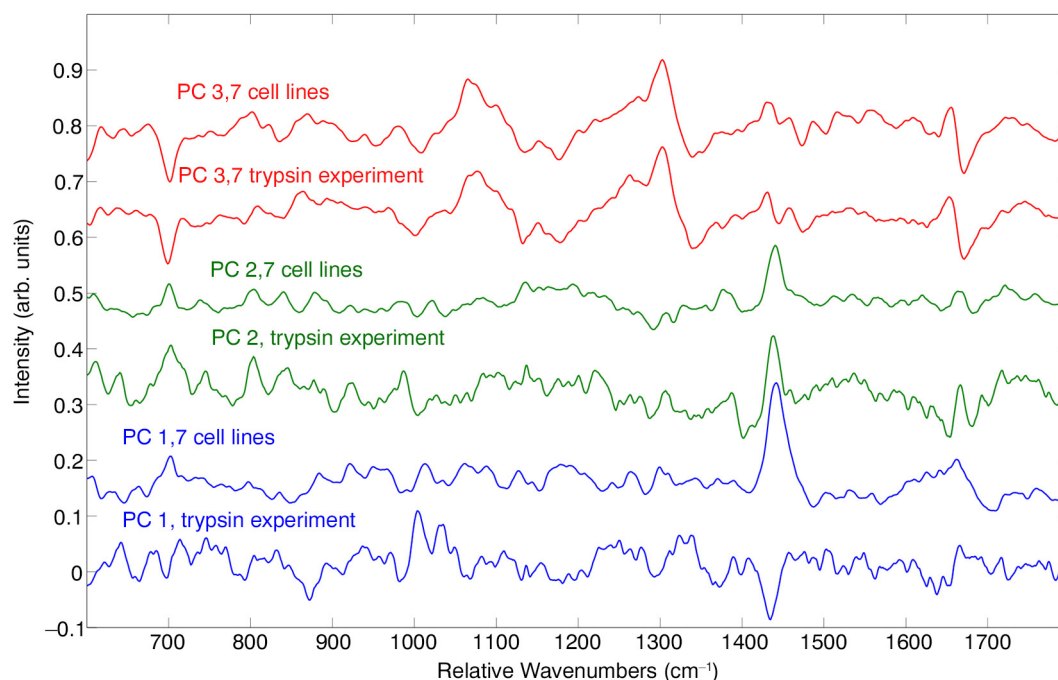
Zachary J. Smith et al.

Fig. 6. Comparison of the first 3 principal component loadings from the trypsin and cell line experiments. Spectra are offset for clarity.

However, LTRS does have some limitations. Its primary limitation is signal strength. Raman scattering is a weak process, generally considered to be on the order of 1 million times weaker than fluorescence labelling. This necessitates long integration times (~ 5 min in our experiments) to measure a spectrum from a single exosome. Furthermore, as discussed in the Supplementary File, because we use bright-field imaging to find and trap exosomes, we are likely biased to looking at exosomes of approximately 100 nm and larger. As signal scales with the cube of the radius, measuring smaller exosomes may require even longer integration times. However, many groups are currently researching methods to speed up measurements by multiplexing measurements (57) or employing "smart" detection strategies (58–61). These advances may make LTRS more approachable as a general analysis technique for exosomes. Another limitation of Raman spectroscopy is that, in complex chemical mixtures such as cells or exosomes, it is difficult for Raman spectroscopy to differentiate between many proteins, especially those at very low concentrations. Therefore, many Raman studies limit themselves to quantifying broad classes of molecules (total protein content, total lipid content, total nucleic acid content, etc.), rather than quantifying the amount of a particular biomolecule (e.g. CD63). We must be careful, then, to limit our conclusions to the information provided by Raman spectroscopy. In the quantitative analysis we present above, we hypothesize that Raman spectroscopy reports on an exosome's surface protein expression level. However, here we must clearly highlight the fact that 2 exosomes may have identical amounts of surface protein, yet be expressing very different types of protein, and Raman spectroscopy may not be able to provide that more detailed information.

Additionally, our experiments also have some limitations. In this study, no density gradient purification steps were performed, and thus protein aggregates or other contaminants may have been present in our sample. However, we would expect such particles to have quite different Raman spectral signatures from exosomes that were not observed in the particles we studied. Nevertheless, we cannot fully eliminate the possibility of these aggregates contaminating our measurements. In performing our experiments, and as detailed in the Supplementary File, we have acquired extensive circumstantial evidence that the measurements we make arise from single exosomes. This evidence comes from confirming our ability to trap and record signals from standard particles in the exosome size range, substantiating via nanoparticle tracking analysis (NTA) that no or few particles exist in our samples outside the exosome size range. This point confirms that we can observe discrete jumps and drops in signal as exosomes enter and leave our laser trap; it shows that our exosome signal for our recorded measurements does not fluctuate over time (as might be expected from multiple exosomes entering the trap). However, we have no direct measurements of the size of the particles measured within the optical trap, and thus the presence of clusters of small numbers of exosomes cannot be rigorously excluded. Despite these limitations, the work described here demonstrates that Raman spectroscopy has

significant power in quantitatively analysing molecules on a single-to-few-exosome level.

A major finding of this study is the observation of significant variation in the chemical content of EVs reported by Raman spectroscopy. For example, Fig. 5 clearly shows the separation by Raman spectroscopy between exosomes and MVs released from the same cell culture, as prepared by differential centrifugation. Figure 3 also demonstrates that among exosomes from different cell lines, there are strong similarities among the spectra, yet consistent spectral differences that lead to grouping of exosomes into 4 major subpopulations by a hierarchical clustering analysis. These subpopulations are not due to different cell origin, as many cell lines have exosomes in many subpopulations, and all subpopulations contain exosomes from multiple cell lines. Yet, there are some subgroups of exosomes that are preferred by some cell lines versus others. For example, exosomes from non-cancerous cells primarily fall into subgroups 2 and 3. This suggests that each subtype of exosome may play a particular functional role that is common across cell lines.

A principal components analysis of this data set yields insights into the chemical differences between the different EV subpopulations. The second major finding of this study is that these differences are primarily due to membrane content of the EVs. The shapes of the first and third principal components are closely matched with spectra of known membrane constituents. Namely, the first principal component has a spectral shape very similar to that of cholesterol, while the third principal component represents the inverse relationship between cholesterol content and phospholipid content in the membrane, as confirmed by fitting this lineshape to pure chemical spectra. Therefore, increasing values along the PC_{7c} 1 axis corresponds to increasing cholesterol content, while increasing values along the PC_{7c} 3 axis corresponds to increased phospholipid content at the expense of cholesterol, with a 1:1 molecular substitution ratio. Notably, non-cancerous cell-derived exosomes seem to be much more enriched in cholesterol, while being relatively depleted in phospholipid, compared to cancerous cell-derived exosomes. This is the first time the content of EV membranes has been examined at the individual vesicle level, highlighting the fact that achieving this level of quantitative chemical detail at the single vesicle level would be difficult or impossible using conventional methods of exosome chemical analysis. However, it is relatively straightforward with LTRS given its linear relationship to chemical components within the few femtolitre measurement volume.

Treating EVs with trypsin cleaves the external domain of most membrane proteins, leading to an expected alteration in the Raman spectra of these vesicles. Comparing native and treated EVs, native exosomes and MVs are clearly distinguished by their Raman spectra, whereas trypsin-treated ones are not. This difference suggests that these vesicles are distinguished primarily by their membrane components that are altered by trypsinization, such as tetraspanins as shown in the Western blots in Fig. 2c. Furthermore, analysis of trypsin-treated and native EVs leads to the construction of principal components that bear a strong resemblance to those constructed through analysis of exosomes from several different cell lines, discussed above. In particular, the second principal component from the 7 cell line experiment (PC_{7c} 2) can be well-fit by the first and second principal components of the trypsin experiment (PC_{Tr} 1 and 2), lending significant confidence to the conclusion that PC_{7c} 2 reports on surface protein expression, with increasing values along this axis corresponding to decreased surface protein content. Meanwhile, cholesterol content, which PC_{7c} 1 demonstrated to be a key variable among exosomes from different cell lines, was not a significant contributor to the separation between exosomes and MVs from a single cell line.

As mentioned above, Raman spectroscopy has limited speed, meaning that our analysis is necessarily limited to relatively small numbers of exosomes. Measuring a very large number of exosomes could ensure a more robust and accurate representation of the true spectral variation within the data set, compared to noise-induced variations. However, comparing the results of the 7 cell line experiment with the trypsin experiment, we are encouraged by the similarities of the principal components analysis of these 2 independent data sets. Each spectral decomposition was performed using different numbers of measured exosomes, yet the spectral shapes of the first few principal components were largely preserved. This result suggests that these early principal components are quite robust despite the modest number of exosomes studied in total.

Our study highlights the need for the development of new analytical techniques that can study individual vesicles. In light of the observed vesicle-to-vesicle heterogeneity, bulk measurements of EVs may not be enough to fully understand their biological function and variability. Our data demonstrate the existence of multiple populations of exosomes shared among cell lines and suggest further studies aimed at taking vesicles grouped by Raman spectroscopy, or other physical or chemical separation methods, and subjecting them to further analysis to determine the differences in intravesicle cargo and membrane protein content of exosomes produced by even a single cell line. Such studies could help elucidate the various functional relationships between an exosome's construction and the ultimate role it plays in cell function, cellular communication, and, for cancerous cells, carcinogenesis.

Acknowledgements

Zachary J. Smith et al.

University Nanomicroscopy Center (Espoo, Finland) for use of their Cryo-electron microscope.

References

1. Valadi H, Ekstrom K, Bossios A, Sjostrand M, Lotvall J. Exosomes contain a selective number of mRNA and micro-RNA. Allergy. 2007;62:S372.
2. Valadi H, Ekstrom K, Bossios A, Sjostrand M, Lee JJ, Lotvall JO. Exosome-mediated transfer of mRNAs and microRNAs is a novel mechanism of genetic exchange between cells. Nat Cell Biol. 2007;9:654–9.
3. Lazaro-Ibanez E, Sanz-Garcia A, Visakorpi T, Escobedo-Lucea C, Siljander P, Ayuso-Sacido A, et al. Different gDNA content in the subpopulations of prostate cancer extracellular vesicles: apoptotic bodies, microvesicles, and exosomes. Prostate. 2014;74:1379–90.
4. Kastelowitz N, Yin H. Exosomes and microvesicles: identification and targeting by particle size and lipid chemical probes. Chembiochem. 2014;15:923–8.
5. Bobrie A, Thery C. Exosomes and communication between tumours and the immune system: are all exosomes equal? Biochem Soc Trans. 2013;41:263–7.
6. Beach A, Zhang HG, Ratajczak MZ, Kakar SS. Exosomes: an overview of biogenesis, composition and role in ovarian cancer. J Ovarian Res. 2014;7:14.
7. Melo SA, Sugimoto H, O'Connell JT, Kato N, Villanueva A, Vidal A, et al. Cancer exosomes perform cell-independent microRNA biogenesis and promote tumorigenesis. Cancer Cell. 2014;26:707–21.
8. Liang Y, Eng WS, Colquhoun DR, Dinglasan RR, Graham DR, Mahal LK. Complex N-linked glycans serve as a determinant for exosome/microvesicle cargo recruitment. J Biol Chem. 2014;289:32526–37.
9. Subra C, Grand D, Laulagnier K, Stella A, Lambeau G, Paillasse M, et al. Exosomes account for vesicle-mediated transcellular transport of activatable phospholipases and prostaglandins. J Lipid Res. 2010;51:2105–20.
10. Laulagnier K, Motta C, Hamdi S, Roy S, Fauvelle F, Pageaux JF, et al. Mast cell- and dendritic cell-derived exosomes display a specific lipid composition and an unusual membrane organization. Biochem J. 2004;380:161–71.
11. Lotvall J, Hill AF, Hochberg F, Buzas EI, Di Vizio D, Gardiner C, et al. Minimal experimental requirements for definition of extracellular vesicles and their functions: a position statement from the International Society for Extracellular Vesicles. J Extracell Vesicles. 2014;3:26913, doi: http://dx.doi.org/10.3402/jev.v3.26913
12. Puppels GJ, Demul FFM, Otto C, Greve J, Robertnicoud M, Arndtjovin DJ, et al. Studying single living cells and chromosomes by confocal Raman microspectroscopy. Nature. 1990; 347:301–3.
13. de Oliveira MAS, Smith ZJ, Knorr F, de Araujo RE, Wachsmann-Hogiu S. Long term Raman spectral study of power-dependent photodamage in red blood cells. Appl Phys Lett. 2014;104:103702.
14. Smith ZJ, Chang CW, Lawson LS, Lane SM, Wachsmann-Hogiu S. Precise monitoring of chemical changes through localization analysis of dynamic spectra (LADS). Appl Spectrosc. 2013;67:187–95.
15. Haka AS, Shafer-Peltier KE, Fitzmaurice M, Crowe J, Dasari RR, Feld MS. Diagnosing breast cancer by using Raman spectroscopy. Proc Natl Acad Sci USA. 2005;102:12371–6.
16. Lieber CA, Majumder SK, Billheimer D, Ellis DL, Mahadevan-Jansen A. Raman microspectroscopy for skin cancer detection in vitro. J Biomed Opt. 2008;13:024013.
17. Schulmerich MV, Cole JH, Kreider JM, Esmonde-White F, Dooley KA, Goldstein SA, et al. Transcutaneous Raman Spectroscopy of Murine Bone In Vivo. Appl Spectrosc. 2009; 63:286–95.
18. Maher JR, Takahata M, Awad HA, Berger AJ. Raman spectroscopy detects deterioration in biomechanical properties of bone in a glucocorticoid-treated mouse model of rheumatoid arthritis. J Biomed Opt. 2011;16:087012.
19. Moritz TJ, Taylor DS, Polage CR, Krol DM, Lane SM, Chan JW. Raman spectroscopic signatures of the metabolic states of *Escherichia coli* cells and their dependence on antibiotics treatment. Biophys J. 2010;98:742A.
20. Berger AJ, Koo TW, Itzkan I, Horowitz G, Feld MS. Multi-component blood analysis by near-infrared Raman spectroscopy. Appl Optics. 1999;38:2916–26.
21. Qi DH, Berger AJ. Chemical concentration measurement in blood serum and urine samples using liquid-core optical fiber Raman spectroscopy. Appl Optics. 2007;46:1726–34.
22. Wachsmann-Hogiu S, Weeks T, Huser T. Chemical analysis in vivo and in vitro by Raman spectroscopy – from single cells to humans. Curr Opin Biotechnol. 2009;20:63–73.
23. Smith ZJ, Huser TR, Wachsmann-Hogiu S. Raman scattering in pathology. Anal Cell Pathol (Amst). 2012;35:145–63.
24. Chen K, Qin YJ, Zheng F, Sun MH, Shi DR. Diagnosis of colorectal cancer using Raman spectroscopy of laser-trapped single living epithelial cells. Opt Lett. 2006;31:2015–7.
25. Chan JW, Taylor DS, Lane SM, Zwerdling T, Tuscano J, Huser T. Nondestructive identification of individual leukemia cells by laser trapping Raman spectroscopy. Anal Chem. 2008;80: 2180–7.
26. Smith ZJ, Wang JCE, Quataert SA, Berger AJ. Integrated Raman and angular scattering microscopy reveals chemical and morphological differences between activated and nonactivated CD8+T lymphocytes. J Biomed Opt. 2010;15:036021.
27. Argov N, Wachsmann-Hogiu S, Freeman SL, Huser T, Lebrilla CB, German JB. Size-dependent lipid content in human milk fat globules. J Agr Food Chem. 2008;56:7446–50.
28. Ajito K, Torimitsu K. Single nanoparticle trapping using a Raman Tweezers microscope. Appl Spectrosc. 2002;56:541–4.
29. Ajito K, Torimitsu K. Laser trapping and Raman spectroscopy of single cellular organelles in the nanometer range. Lab Chip. 2002;2:11–4.
30. Tatischeff I, Larquet E, Falcon-Perez JM, Turpin PY, Kruglik SG. Fast characterisation of cell-derived extracellular vesicles by nanoparticles tracking analysis, cryo-electron microscopy, and Raman tweezers microspectroscopy. J Extracell Vesicles. 2012;1:19179, doi: http://dx.doi.org/10.3402/jev.v1i0.19179
31. Beier BD. Thesis: confocal Raman microscpectroscopy of oral Streptococci. Institute of Optics. Rochester, NY, USA: University of Rochester; 2011.

32. Eilers PH. A perfect smoother. Anal Chem. 2003;75:3631–6.

33. Boelens HF, Dijkstra RJ, Eilers PH, Fitzpatrick F, Westerhuis JA. New background correction method for liquid chromatography with diode array detection, infrared spectroscopic detection and Raman spectroscopic detection. J Chromatogr A. 2004;1057:21–30.

34. Schie IW, Nolte L, Pedersen TL, Smith Z, Wu J, Yahiatene I, et al. Direct comparison of fatty acid ratios in single cellular lipid droplets as determined by comparative Raman spectroscopy and gas chromatography. Analyst. 2013;138:6662–70.

35. Gniadecka M, Philipsen PA, Sigurdsson S, Wessel S, Nielsen OF, Christensen DH, et al. Melanoma diagnosis by Raman spectroscopy and neural networks: structure alterations in proteins and lipids in intact cancer tissue. J Invest Dermatol. 2004;122:443–9.

36. Tirinato L, Gentile F, Di Mascolo D, Coluccio ML, Das G, Liberale C, et al. SERS analysis on exosomes using super-hydrophobic surfaces. Microelectron Eng. 2012;97:337–40.

37. Thery C, Amigorena S, Raposo G, Clayton A. Isolation and characterization of exosomes from cell culture supernatants and biological fluids. Curr Protoc Cell Biol. 2006;Chapter 3:Unit 3 22.

38. Shelke GV, Lasser C, Gho YS, Lotvall J. Importance of exosome depletion protocols to eliminate functional and RNA-containing extracellular vesicles from fetal bovine serum. J Extracell Vesicles. 2014;3:24783, doi: http://dx.doi.org/10.3402/jev.v3.24783

39. Jang SC, Kim OY, Yoon CM, Choi DS, Roh TY, Park J, et al. Bioinspired exosome-mimetic nanovesicles for targeted delivery of chemotherapeutics to malignant tumors. ACS Nano. 2013;7:7698–710.

40. Boing AN, van der Pol E, Grootemaat AE, Coumans FA, Sturk A, Nieuwland R. Single-step isolation of extracellular vesicles by size-exclusion chromatography. J Extracell Vesicles. 2014;3:23430, doi: http://dx.doi.org/10.3402/jev.v3.23430

41. Webber J, Clayton A. How pure are your vesicles? J Extracell Vesicles. 2013;2:19861, doi: http://dx.doi.org/10.3402/jev.v2i0.19861

42. Dragovic RA, Gardiner C, Brooks AS, Tannetta DS, Ferguson DJ, Hole P, et al. Sizing and phenotyping of cellular vesicles using nanoparticle tracking analysis. Nanomed-Nanotechnol. 2011;7:780–8.

43. Filipe V, Hawe A, Jiskoot W. Critical evaluation of nanoparticle tracking analysis (NTA) by NanoSight for the measurement of nanoparticles and protein aggregates. Pharm Res. 2010;27:796–810.

44. Maas SL, de Vrij J, van der Vlist EJ, Geragousian B, van Bloois L, Mastrobattista E, et al. Possibilities and limitations of current technologies for quantification of biological extracellular vesicles and synthetic mimics. J Control Release. 2015;200:87–96.

45. Krafft C, Neudert L, Simat T, Salzer R. Near infrared Raman spectra of human brain lipids. Spectrochim Acta A. 2005;61:1529–35.

46. Naumann D. Infrared and NIR Raman spectroscopy in medical microbiology. Proc Soc Photo-Opt Ins. 1998;3257:245–57.

47. Miura T, Takeuchi H, Harada I. Characterization of individual tryptophan side-chains in proteins using Raman-spectroscopy and hydrogen-deuterium exchange kinetics. Biochemistry. 1988;27:88–94.

48. Edwards HGM, Farwell DW, Williams AC, Barry BW, Rull F. Novel spectroscopic deconvolution procedure for complex biological-systems – vibrational components in the Ft-Raman spectra of ice-man and contemporary skin. J Chem Soc Faraday Trans. 1995;91:3883–7.

49. Notingher I, Verrier S, Haque S, Polak JM, Hench LL. Spectroscopic study of human lung epithelial cells (A549) in culture: living cells versus dead cells. Biopolymers. 2003;72:230–40.

50. Nijssen A, Schut TCB, Heule F, Caspers PJ, Hayes DP, Neumann MHA, et al. Discriminating basal cell carcinoma from its surrounding tissue by Raman spectroscopy. J Invest Dermatol. 2002;119:64–9.

51. Huang ZW, McWilliams A, Lui H, McLean DI, Lam S, Zeng HS. Near-infrared Raman spectroscopy for optical diagnosis of lung cancer. Int J Cancer. 2003;107:1047–52.

52. Raposo G, Stoorvogel W. Extracellular vesicles: exosomes, microvesicles, and friends. J Cell Biol. 2013;200:373–83.

53. Buschman HP, Deinum G, Motz JT, Fitzmaurice M, Kramer JR, van der Laarse A, et al. Raman microspectroscopy of human coronary atherosclerosis: biochemical assessment of cellular and extracellular morphologic structures in situ. Cardiovasc Pathol. 2001;10:69–82.

54. Rodriguez J, Gupta N, Smith RD, Pevzner PA. Does trypsin cut before proline? J Proteome Res. 2008;7:300–5.

55. Huang HL, Hsing HW, Lai TC, Chen YW, Lee TR, Chan HT, et al. Trypsin-induced proteome alteration during cell sub-culture in mammalian cells. J Biomed Sci. 2010;17:36.

56. Lee C, Carney RP, Hazari S, Smith ZJ, Knudson A, Robertson CS, et al. 3D plasmonic nanobowl platform for the study of exosomes in solution. Nanoscale. 2015;7:9290–7.

57. Kong LB, Chan J. A rapidly modulated multifocal detection scheme for parallel acquisition of Raman spectra from a 2-D focal array. Anal Chem. 2014;86:6604–9.

58. Smith ZJ, Strombom S, Wachsmann-Hogiu S. Multivariate optical computing using a digital micromirror device for fluorescence and Raman spectroscopy. Opt Express. 2011;19:16950–62.

59. Kosmeier S, Zolotovskaya S, De Luca AC, Riches A, Herrington CS, Dholakia K, et al. Nonredundant Raman imaging using optical eigenmodes. Optica. 2014;1:257–63.

60. Wilcox DS, Buzzard GT, Lucier BJ, Wang P, Ben-Amotz D. Photon level chemical classification using digital compressive detection. Anal Chim Acta. 2012;755:17–27.

61. Davis BM, Hemphill AJ, Maltas DC, Zipper MA, Wang P, Ben-Amotz D. Multivariate hyperspectral Raman imaging using compressive detection. Anal Chem. 2011;83:5086–92.